International Journal of Nanomedicine

Dovepress
open access to scientific and medical research

Open Access Full Text Article

ORIGINAL RESEARCH

In vitro and in vivo evaluations of nanocrystalline Zn-doped carbonated hydroxyapatite/alginate microspheres: zinc and calcium bioavailability and bone regeneration

This article was published in the following Dove Press journal:
International Journal of Nanomedicine

International Journal of Nanomedicine downloaded from https://www.dovepress.com/
For personal use only.

Victor R Martinez-Zelaya[1,*]
Laila Zarranz[2,*]
Edher Z Herrera[1,*]
Adriana T Alves[2]
Marcelo José Uzeda[2]
Elena Mavropoulos[1]
André L Rossi[1]
Alexandre Mello[1]
José M Granjeiro[2,3]
Monica D Calasans-Maia[2]
Alexandre M Rossi[1]

[1]Department of Condensed Matter, Applied Physics and Nanoscience, Brazilian Center for Research in Physics, Rio de Janeiro, RJ, Brazil; [2]Dental Clinical Research Center, Oral Diagnosis Department and Oral Surgery Department, Dentistry School, Fluminense Federal University, Niteroi, RJ, Brazil; [3]National Institute of Metrology, Quality and Technology, Duque de Caxias, RJ, Brazil

*These authors contributed equally to this work

Background: Zinc-doped hydroxyapatite has been proposed as a graft biomaterial for bone regeneration. However, the effect of zinc on osteoconductivity is still controversial, since the release and resorption of calcium, phosphorus, and zinc in graft-implanted defects have rarely been studied.

Methods: Microspheres containing alginate and either non-doped carbonated hydroxyapatite (cHA) or nanocrystalline 3.2 wt% zinc-doped cHA (Zn-cHA) were implanted in critical-sized calvarial defects in Wistar rats for 1, 3, and 6 months. Histological and histomorphometric analyses were performed to evaluate the volume density of newly formed bone, residual biomaterial, and connective tissue formation. Biomaterial degradation was characterized by transmission electron microscopy (TEM) and synchrotron radiation-based X-ray microfluorescence (SR-μXRF), which enabled the elemental mapping of calcium, phosphorus, and zinc on the microsphere-implanted defects at 6 months post-implantation.

Results: The bone repair was limited to regions close to the preexistent bone, whereas connective tissue occupied the major part of the defect. Moreover, no significant difference in the amount of new bone formed was found between the two microsphere groups. TEM analysis revealed the degradation of the outer microsphere surface with detachment of the nanoparticle aggregates. According to SR-μXRF, both types of microspheres released high amounts of calcium, phosphorus, and zinc, distributed throughout the defective region. The cHA microsphere surface strongly adsorbed the zinc from organic constituents of the biological fluid, and phosphorus was resorbed more quickly than calcium. In the Zn-cHA group, zinc and calcium had similar release profiles, indicating a stoichiometric dissolution of these elements and non-preferential zinc resorption.

Conclusions: The nanometric size of cHA and Zn-cHA was a decisive factor in accelerating the in vivo availability of calcium and zinc. The high calcium and zinc accumulation in the defect, which was not cleared by the biological medium, played a critical role in inhibiting osteoconduction and thus impairing bone repair.

Keywords: zinc-doped carbonated hydroxyapatite, nanocomposite, synchrotron radiation-based X-ray microfluorescence, zinc/calcium bioavailability, bone regeneration

Correspondence: Alexandre M Rossi; Victor R Martinez-Zelaya
Brazilian Center for Research in Physics (CBPF). Rio de Janeiro 22290-180, RJ, Brazil
Tel +55 212 141 7310
Email rossi@cbpf.br; victormz@cbpf.br

Introduction

Calcium phosphates (CPs), such as hydroxyapatite (HA), have been extensively used in dentistry and medicine for the repair of bone tissue damaged by trauma, tumors, infections, and congenital abnormalities. Because of their excellent

© 2019 Martinez-Zelaya et al. This work is published and licensed by Dove Medical Press Limited. The full terms of this license are available at https://www.dovepress.com/terms.php and incorporate the Creative Commons Attribution – Non Commercial (unported, v3.0) License (http://creativecommons.org/licenses/by-nc/3.0/). By accessing the work you hereby accept the Terms. Non-commercial uses of the work are permitted without any further permission from Dove Medical Press Limited, provided the work is properly attributed. For permission for commercial use of this work, please see paragraphs 4.2 and 5 of our Terms (https://www.dovepress.com/terms.php).

biocompatibility and osteoconductivity, nanostructured HA and HA-based composites with different polymers have been widely investigated for their application in the field of bone tissue engineering.[1–7]

Significant research has been carried out in the field of substituted apatites to improve HA osteoconduction.[8] The presence of carbonates in the HA structure decreases the latter's crystallinity, resulting in an increase in the in vitro and in vivo solubilities of the biomaterial, with a higher presence of neo-formed bone. Zinc (Zn), an essential trace element in the body, has stimulatory effects on bone formation both in vitro and in vivo as well as an inhibitory effect on osteoclastic bone resorption in vitro.[9]

Despite a large number of in vitro and in vivo studies on Zn-doped CPs, the role of Zn substitution on the osteoconduction properties of HA remains controversial. Recently, Cruz et al[10] published a systematic review of 18 in vivo studies that reported the effect of Zn incorporation into CPs, with consideration of material biocompatibility, Zn resorption, and bone repair efficiency. The analysis of the results was not conclusive owing to the variability of experimental conditions, such as the i) animal models used, ii) site of implantation, iii) experimental periods, iv) nature and fabrication method of the Zn-doped CPs, and v) Zn concentrations. All of the studies found Zn-CP to be biocompatible, and eight studies suggested that Zn stimulated bone repair,[11–18] whereas four claimed that Zn-doped CP behaved similarly to non-doped CP.[9,19–21] However, two studies showed opposite results with regard to osteoinduction in intramuscular models, with one obtaining negative effects using Zn-HA in rabbits[22] and the other demonstrating positive effects using Zn-containing tricalcium phosphate in canines.[23] In general, the studies considered that Zn bioavailability was an essential parameter for bone repair, and Zn-doping reduced the resorption of the biomaterial.

This present study aimed to evaluate the osteoconduction behavior of microspheres produced from nanostructured Zn-doped carbonated hydroxyapatite (Zn-cHA), in critical-sized calvarial defects in the rat. Synchrotron radiation-based X-ray microfluorescence (SR-μXRF) and transmission electron microscopy (TEM) were used to analyze the in vivo release and resorption of calcium (Ca), phosphorus (P), and Zn in the microsphere-implanted defect and the possible relationship with bone repair.

Materials and methods

Synthesis of cHA and Zn-cHA powders and microsphere preparation

The cHA and Zn-cHA powders (atomic ratio: Zn/Ca=0.5 and CO_3/PO_4=0.17) were precipitated through dropwise addition of an aqueous $(NH_4)_2HPO_4$ solution to a solution containing $Ca(NO_3)_2$, $Ca(CO_3)_2$, and $Zn(NO_3)_2$ at a pH of 9.0, followed by stirring of the suspension for 3 h at 90 °C. The precipitate was then separated by filtration, repeatedly washed with boiling deionized water, and subsequently dried at 100 °C for 24 h. The dried powder was ground manually and particles of <210 μm in size were then separated by sieving. The cHA or Zn-cHA powders were gently dispersed in a 10 mg/mL aqueous solution of sodium alginate to achieve an alginate/powder ratio of 1:15 (6.7 wt% of alginate). The alginate/powder mixture was extruded dropwise at room temperature into a 0.15 M $CaCl_2$ solution, using a needle of 0.70 mm diameter. Microspheres formed instantaneously and were allowed to mature in the $CaCl_2$ solution for 24 h for complete gelation. The cHA and Zn-cHA microspheres were dried overnight in an oven at 30 °C.

Sample characterization

The cHA and Zn-cHA powders and microspheres were characterized by atomic absorption spectroscopy (AAS), UV-Vis spectrophotometry, X-ray diffraction (XRD), scanning electron microscopy (SEM), and Fourier-transform infrared (FTIR) spectroscopy. The Ca and Zn contents of the precipitated powders were determined by quantitative chemical analysis using AAS on a Shimadzu 6800 instrument (Shimadzu, Kyoto, Japan). The phosphate content was determined by the vanadomolybdate phosphoric acid colorimetric method, using a UV-Vis spectrophotometer (Shimadzu UV-2450) at 420 nm. For determination of the carbonate content, the powdered samples were subjected to an oxy-reduction process in an oven at 1350 °C with an atmosphere of superdry oxygen, and the carbon present in the sample was then converted to CO_2 (SC-144DR Sulfur and Carbon Analyzer; LECO Corp., Saint Joseph, MI, USA). The surface area and pore size were determined by the Brunauer–Emmett–Teller (BET) method, using the Accelerated Surface Area and Porosimetry System (ASAP 2020; Micromeritics, Norcross, GA, USA).[24,25]

The microparticles were embedded in epoxy resin (EPON) and polymerized at 60 °C for 48 h. The resin was then mounted on aluminum stubs and polished. The samples were coated with a thin gold layer, and a carbon

tape was attached to the sample to avoid charging during the SEM analysis.

Images were acquired using an LYRA-3 workstation (TESCAN, Brno, Czech Republic), equipped with an energy-dispersive X-ray spectrometer (EDS) (Oxford Instruments, High Wycombe, UK). SEM images were acquired by applying a voltage of 10 kV and using a backscattered electron detector (Oxford Instruments). The dimensions of the recorded images were 1024×1144 pixels and the dwell time was 30 µs/pixel.

SR-µXRF and synchrotron radiation-based X-ray microtomography (SR-µCT) were also used for the analysis. The experiments were carried out with the X-ray fluorescence microprobe available at the D09B XRF beamline of the Brazilian Synchrotron Light Laboratory (LNLS) at Campinas, Brazil.[26] An X-ray optic based on a pair of dynamically figured mirrors in a so-called KB mirror arrangement was used. The X-ray focusing system (fabricated by the X-ray Optic Group of the European Synchrotron Radiation Facility (ESRF) in Grenoble, France)[27] can produce an X-ray microbeam of approximately 12 µm×22 µm in size. Measurements were performed under normal temperature and pressure conditions. An aluminum filter was placed in front of the incoming beam to reduce distortion of the SR-XRF spectra due to the high X-ray fluorescence intensity of the Ca-K lines coming from the sample matrix. Samples were put in the focus plane with an accuracy of 1 µm, with precise remote-controlled motorized stages. An optical microscope (magnification of ~500×) was used to precisely locate the irradiated areas. The 2D-XRF maps were generated (30 µm steps) in a continuous scanning mode of operation ("on-the-fly" scans)[28] on areas covering specific regions of the mineralized tissue. The elemental composition per pixel was determined at a standard geometry (45–45°), using a silicon drift detector (KETEK GmbH, Munich, Germany) with a resolution of 140 eV (FWHM) at 5.9 keV. Spectra processing and elemental imaging reconstructions were done with PyMca software.[29] Semi-quantitative analysis of the XRF spectra was done using a reference sample of calvarial bone (area of 16×16 in pixel size). The fundamental parameters method was used to determine the elemental concentration in the bone matrix.[30] The X-ray absorption factor used was A=1 (thin film condition), owing to the small thickness of the samples.[31] The elemental concentration of the calvarial bone and the elemental image model of the samples were estimated from a certified cortical bone (ICRP) material.[32] The quantitative elemental image data of Ca, P, and Zn are given in mass fractions. The RBG tools of PyMca were used to construct the concentration profile, scatter plots, and Ca/P and Zn/Ca images pixel by pixel.

SR-µCT was used to characterize the internal structures of the cHA and Zn-cHA microspheres. The samples were analyzed with a micro X-ray scanned at the high-resolution imaging beamline (IMX) at LNLS. The samples were illuminated by a polychromatic beam (4–24 keV), and a 550µm silicon filter was positioned before the sample to reduce the beam-hardening effect.[33] A total of 1001 projections were captured using a CCD camera (PCO.2000), and a 10× lens was used to magnify the images and obtain a pixel size of 0.82 µm. The experiments were performed in contrast mode, and the count mode was used to ensure the same flux on all projections, as the beam current had a half-time of 12 h, which changed considerably during the experiment (typically, one full 3D scan takes 45 min). A fast back-projection algorithm reconstructed the data,[34–36] and FIJI software[37] was used to select and crop the region of interest. Avizo 9.5, a 3D visualization software, was used to filter, segment, and analyze the images. The data processing in Avizo 9.5 started by applying a non-local means filter, which was used as a post-reconstruction filter to reduce artefacts.[38] The Magic Wand tool was used to perform a quick segmentation of the microspheres, pores, and background phases, as determined by their corresponding threshold range. These images were further fine-tuned using the watershed segmentation tool,[39] to achieve an accurate segmentation. Thus, we were able to calculate the volume fraction of each phase. To determine the equivalent pore diameter, the corresponding phase (pore) was isolated; applying the separate objects tool, each pore was individualized and separated from its corresponding pore throat.[40,41] The equivalent diameter q_i was obtained as follows:

$$q_i = \sqrt[3]{\frac{6 \times V3d_i}{\pi}} \quad (1)$$

where $V3d_i$ is the volume of each individual pore quantized.

The cHA and Zn-cHA microspheres were analyzed by TEM after 6 months of implantation. The samples were first fixed with glutaraldehyde (2.5%) and paraformaldehyde (4%) in cacodylate buffer (0.1 M, pH 7.3), and then washed in cacodylate buffer, dehydrated in acetone (in solutions from 30% to 100%), and embedded in epoxy resin at 70 °C for 24 h. Ultrathin sections were obtained in an ultramicrotome (PT-XL PowerTome, RMC Boeckeler,

Tuscon, AZ, USA) using a diamond knife. The sections were analyzed in a JEOL 2100F transmission electron microscope operated at 200 kV. Images and selected area electron diffraction (SAED) patterns were recorded with an 11 megapixel CCD camera (Orius; GATAN Inc., Pleasanton, CA, USA).

Cytocompatibility assay and cell viability

MC3T3-E1 (ATCC 7594), a murine osteoblastic mycoplasm-free cell line, was used in this study. The cells were cultured in alpha-minimum essential medium (α-MEM; Sigma, St. Louis, MO, USA), supplemented with 10% fetal bovine serum (FBS), at 37 °C and 5% CO_2. Co-confluent passages were trypsinized and used in all experiments. cHA and Zn-cHA microsphere extracts were prepared according to the methods described by the International Organization for Standardization.[42] The concentration of each sample in the culture medium was 100 mg/mL. Each sample was incubated at 37 °C for 24 h in α-MEM, supplemented with 10% FBS. The extracts were analyzed using AAS on a Shimadzu 6800 instrument to determine the elemental concentrations of Ca and Zn released.

Extracts of cells treated with cHA or Zn-cHA at different dilutions were analyzed to determine the cytotoxicity of the biomaterials. MC3T3 cells, subcultured on 96-well plates at a density of 1×10^4 cells/well, were exposed to each extract for 24 h at 37 °C and 5% CO_2. Cells cultured under supplemented regular medium were used as the negative control (C–), and a 1% sodium dodecyl sulfate solution was used as the positive control (C+). The cell viability after biomaterial exposure was determined with the PrestoBlue Cell Viability Reagent (Invitrogen, Life Technologies, Carlsbad, CA, USA). Viable cells reduce resazurin to resorufin under cellular respiration, a process that is accompanied by fluorescence changes in the solution. Therefore, measurements of the fluorescence and absorbance of the solution indicate cellular metabolic activity, and consequently the presence of viable cells. After 24 h of cell exposure to each conditioned medium, 20 µL of PrestoBlue was added to each well and the plates were incubated at 37 °C for 30 min. After incubation, the change in the fluorescence (resazurin to resorufin) was measured at 590 nm. Three independent experiments were performed in sextuplicate. The normalized cell viability data (where C–=100%) were submitted to analysis of variance (ANOVA) and Tukey's *post-hoc* test, where a value of $p<0.05$ was considered statistically different from C–. The statistical tests were performed using GraphPad Prism 6.0 (GraphPad Software Inc., San Diego, CA, USA).

In vivo experiments

Ethical considerations

The animal breeding and experiments were performed according to conventional guidelines of the *NIH Guide for the Care and Use of Laboratory Animals* (US National Institutes of Health 85–23, revised 1996), following the Brazilian legislation on animal use in experimental research.[43] This study was reported according to the ARRIVE guidelines, concerning the relevant items.[44] The Institutional Animal Care and Use Committee of Federal Fluminense University, Niteroi, Brazil approved the study, and the animal experiments were carried out during the second half of 2016.

Animals

This study used 36 adult male and female Wistar rats (age: 5–6 months), with a mean weight of 300/400 g, provided by the Laboratory Animals Centre at Fluminense Federal University, Niteroi, Rio de Janeiro, Brazil. The animals were kept in individual cages (n=2) and received water and food *ad libitum* throughout the study. A senior veterinarian monitored the nutritional recommendations, animal care, and pre- and post-operative fasting of the animals.

Surgical procedure

All animals were anesthetized with 3 mL of a solution containing ketamine (1 mL) (Virbac, Jurubatuba, SP, Brazil), xylazine (0.5 mL) (FortDodge, São Cristovão, RJ, Brazil), midazolam (0.6 mL), tramadol (0.2 mL), and saline solution (8.5 mL). During the post-operative period, the rats received analgesia (5 mg/kg meloxicam, subcutaneously) every 24 h, starting on the day of surgery (after the procedure) and for two additional days. The animals were randomly placed into boxes on the basis of their experimental groups according to the graft material: cHA (control group) and Zn-cHA (experimental group).

At approximately 3 min after the anesthetic procedure, trichotomy and antisepsis were conducted with 2% chlorhexidine, following which sterilized surgical drapes were affixed to the division and the frontoparietal site was isolated. A half-moon-shaped incision was made to expose the calvarial bone. Thereafter, a critical-sized defect (8 mm diameter) was made in the calvaria for biomaterial implantation. After subsequent repositioning of the periosteum and epithelium, a simple suture was applied for primary closure of the tissue (5–0, Ethicon, Mononylon; Johnson& Johnson, Machelen, Belgium).

Histological preparation

After 1, 3, and 6 months, six animals from each experimental period in each group were euthanized. The bone blocks from five of the animals of each experimental time were fixed in 10% buffered formalin for 48 h and demineralized for 24 h (Allkimia®, a bone demineralizing solution) before histological processing for paraffin embedding. Paraffin sections of 5 µm thickness were stained with hematoxylin–eosin (HE). The bone block from the remaining rat of each experimental time was fixed in 70% ethanol before dehydration and then exposed to an ascending series of alcohol fractions (50–100%) under agitation and vacuum. Subsequently, these were infiltrated through daily changes of ascending grades of resin (Technovit 7200 VLC; Kulzer, Wehrheim, Germany). Afterwards, the samples were embedded in the same resin, which was then cut in the coronal plane using a macro cutting and grinding technique (Exakt 310 CP series; Exakt Apparatebau, Norderstedt, Germany). The grinding and polishing resulted in slides with a final thickness of 50–100 µm for brightfield and polarized light microscopy analyses, and elemental mapping by SR-µXRF.

Histomorphometric evaluation

The decalcified sections were observed under a light microscope (BX43; Olympus, Tokyo, Japan) with 10× objective lens magnification. Eight non-consecutive images of each specimen section (n=5) were acquired using cellSens software (Tokyo, Japan). The volume density of the newly formed bone (NFB), volume density of the residual biomaterial (BM), and evaluation of connective tissue formation (CT) were determined with Image-Pro Plus 6.0 software (Media Cybernetics, Inc., Rockville, MD, USA) by measuring the area of interest. An experienced observer performed the descriptive histological and histomorphometric evaluations. All histological slides were coded, and the examiner evaluated the slides unbiasedly with regard to the experimental group and experimental periods. Statistical analysis was performed using Prism 8, GraphPad®. The Shapiro–Wilk normality test was used to evaluate the modeling of the dataset by a normal distribution (alpha=0.05). ANOVA was used to test the effects of time and treatment on the outcomes (cell viability, volume density of new bone, biomaterial, and connective tissue). For all analyses, a value of $p<0.05$ was considered statistically significant. The bright field and polarized light microscopy images were obtained using a light microscope (Axioplan; Zeiss, Oberkochen, Germany) with 20× objective lens magnification.

Results

CHA and Zn-cHA powder and microspheres characterization

The chemical compositions of the powders are shown in Table 1. Zn-cHA had a Zn content of 3.2 wt% and a (Ca+Zn)/Ca ratio of 1.66±0.02, whereas cHA had a Ca/P ratio of 1.69±0.02. Small amounts of carbon were associated with the apatite structures (1.1% and 0.3% for cHA and Zn-cHA, respectively). Although the powders had similar specific surface areas, Zn-cHA had a smaller mean pore size.

Both samples showed typical XRD patterns of poorly crystalline apatite phases with preferential growth along the 002 direction and average crystallite sizes of 29 nm (Zn-cHA) and 42 nm (cHA) along 002, as calculated by the Scherrer equation with K=0.89 (Figure 1A).[45] The introduction of Zn contributed to the disorder of the cHA structure and XRD line broadening. The FTIR spectra exhibited OH^- bands at 3575.7 and 632 cm^{-1}, and phosphate bands at 1092 cm^{-1} (ν_3), 1036 cm^{-1} (ν_3), 962 cm^{-1} (ν_1), 603 cm^{-1} (ν_4), and 566 cm^{-1} (ν_4) (Figure 1B). Carbonate bands were found at 876 and 1420–1500 cm^{-1}.

SR-µCT was used to characterize the sphere microstructures. As shown in Figure 2A–D, the microspheres were made up of agglomerates of nanoparticles, and the pore spaces were filled with the alginate polymer. The respective pore volumes for cHA and Zn-cHA were 23.8% and 5%, with average equivalent pore diameters of 5.54 and 2.95 µm, respectively (Figure 3). Both samples showed an irregular surface topography with micrometric roughness, as seen in the SEM images of Figures S1A-D. The Zn-cHA surface presented lower roughness than that of cHA, probably due to its smaller particle size.

Table 1 Physicochemical characteristics of cHA and Zn-cHA powder

Samples	Ca (wt%)	*P* (wt%)	Zn (wt%)	C (wt%)	SA[a], (m^2/g)	PS[a,b] (nm)
cHA	39.9	18.3	–	1.1	91	33
Zn-cHA	37.2	18.4	3.2	0.3	89	18

Notes: [a]Determined by BET; [b]nanometric pores.
Abbreviations: SA, surface area; PS, pore size; BET, Brunauer–Emmett–Teller; Zn-cHA, Zinc-doped carbonated hydroxyapatite.

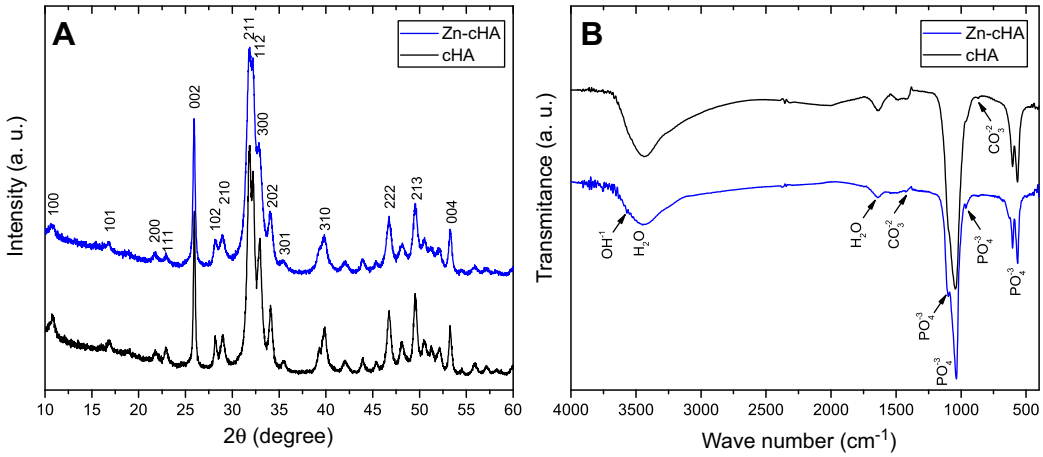

Figure 1 XRD patterns (**A**) and FTIR spectra (**B**) of Zn-cHA and cHA powders.
Abbreviations: XRD, X-ray diffraction; FTIR, Fourier-transform infrared; Zn-cHA, Zinc-doped carbonated hydroxyapatite; cHA, carbonated hydroxyapatite.

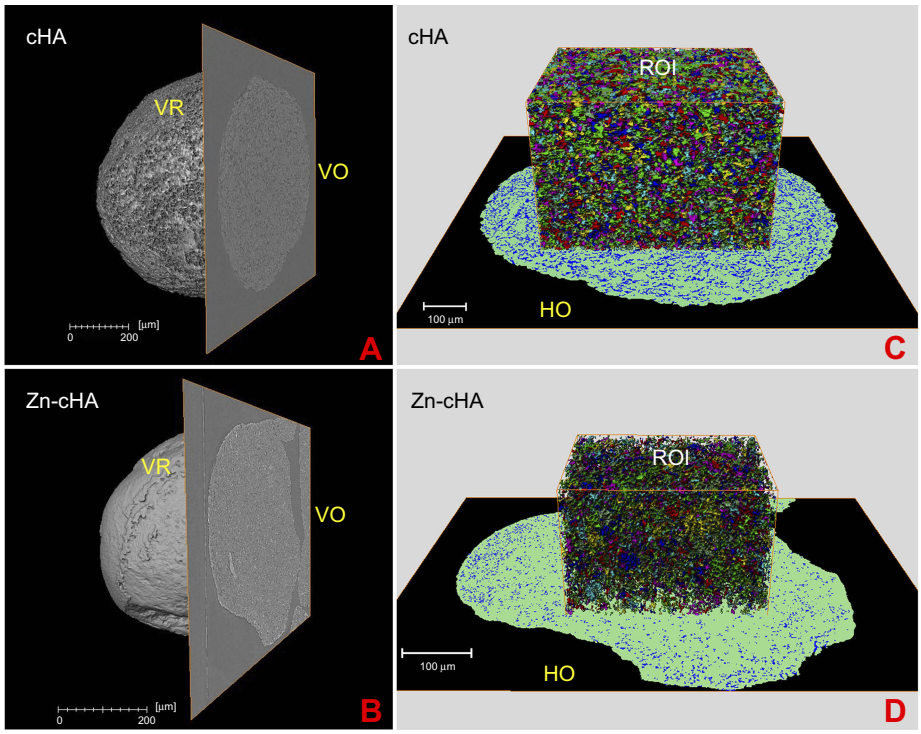

Figure 2 SR-µCT of cHA and Zn-cHA microspheres before implantation. (**A,B**) VR of both cHA and Zn-cHA microspheres with a VO from reconstruction. (**C,D**) ROI box of cHA and Zn-cHA microspheres showing individual pores distribution volume (each color represent the individual pores quantized); and HO of the segmented phases (black: background; green: biomaterial; blue: all pore space).
Abbreviations: SR-µCT, Synchrotron radiation-based X-ray microtomography; cHA, carbonated hydroxyapatite; Zn-cHA, Zinc-doped carbonated hydroxyapatite; VR, volume rendering; VO, vertical orthoslice; HO, horizontal orthoslice; ROI, region of interest.

In vitro cytotoxicity assays

Murine pre-osteoblasts were exposed to culture medium containing Zn-cHA or cHA sample extracts to determine the effect of the biomaterials on cell viability through the use of the PrestoBlue reagent (Figure 4). Cells cultured under these conditions provided a reference for the cytotoxicity of the biomaterials. The assay identified an increase ($p<0.05$, ANOVA and Tukey's test) in metabolic activity for both sample extracts compared with that for the control group. In addition, the statistical analysis indicated that there was no difference between the cells exposed to cHA or Zn-cHA extracts in terms of cell viability.

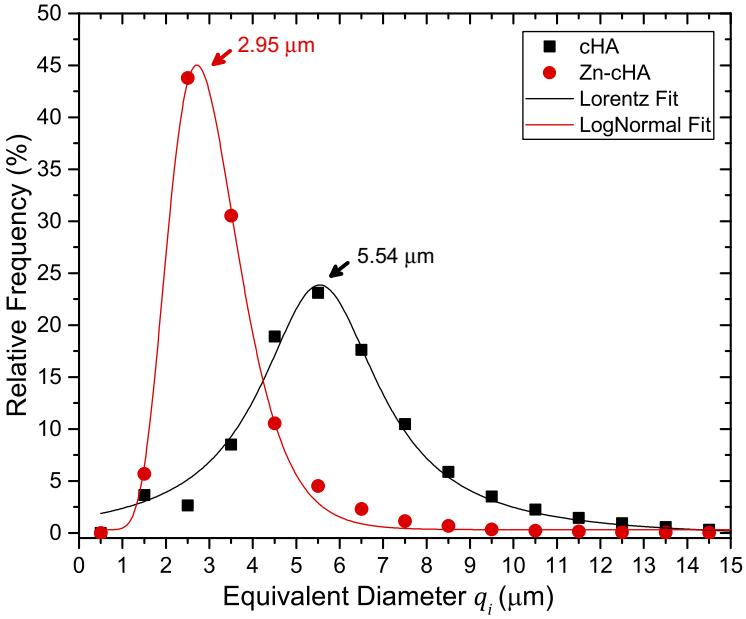

Figure 3 Equivalent micropore diameter (q_i) distribution of non-implanted cHA and Zn-cHA microspheres.
Notes: Fitting model: Lorentz (cHA) and LogNormal (Zn-cHA).
Abbreviations: cHA, carbonated hydroxyapatite; Zn-cHA, Zinc-doped carbonated hydroxyapatite.

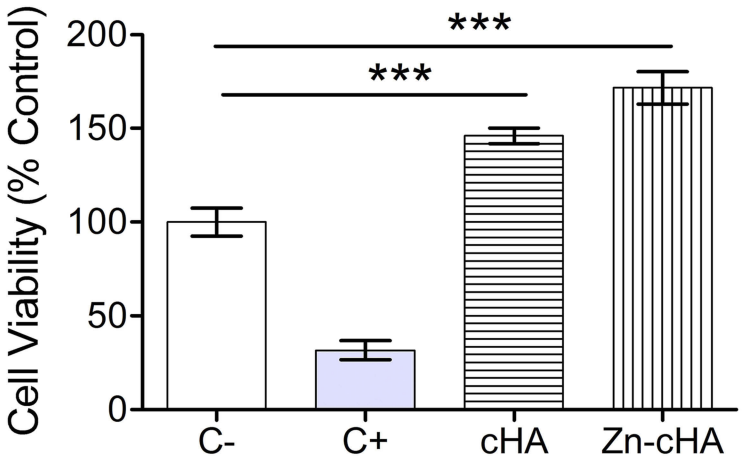

Figure 4 MC3T3 cell viability after exposition to supplemented regular medium, 1% SDS, cHA and Zn-cHA extracts.
Note: (C–, negative control), (C+, positive control). The normalized data (being C– equal to 100%) were submitted to ANOVA with Tukey post-hoc test (*** $p<0.05$) statistically different from C-.
Abbreviations: MC3T3, preosteoblast cells; SDS, sodium dodecyl sulfate; cHA, carbonated hydroxyapatite; Zn-cHA, Zinc-doped carbonated hydroxyapatite.

Histological evaluation and bone regeneration

All animals remained in good health during the healing period and did not develop infections or other post-operative wound-healing complications. The tissue surrounding the biomaterials in the calvaria presented a healthy appearance and did not exhibit any sign of infection or necrosis. The histological evaluation aimed to characterize the biointegration of the biomaterials and the bone repair throughout the experimental periods of 1, 3, and 6 months.

After 1 month of implantation, the defects were filled with fibrous connective tissue with dispersed moderate mononuclear inflammatory infiltrates in both groups. New bone had already formed at the border of the defect, mainly for the Zn-cHA group (Figures 5A and 6A). Sparse inflammatory infiltrates were still observed 3 months after implantation of the cHA and Zn-cHA microspheres. The center of the defects was filled with fibrous connective tissue, whereas newly formed bone was present around the border of the defect. Large areas of residual

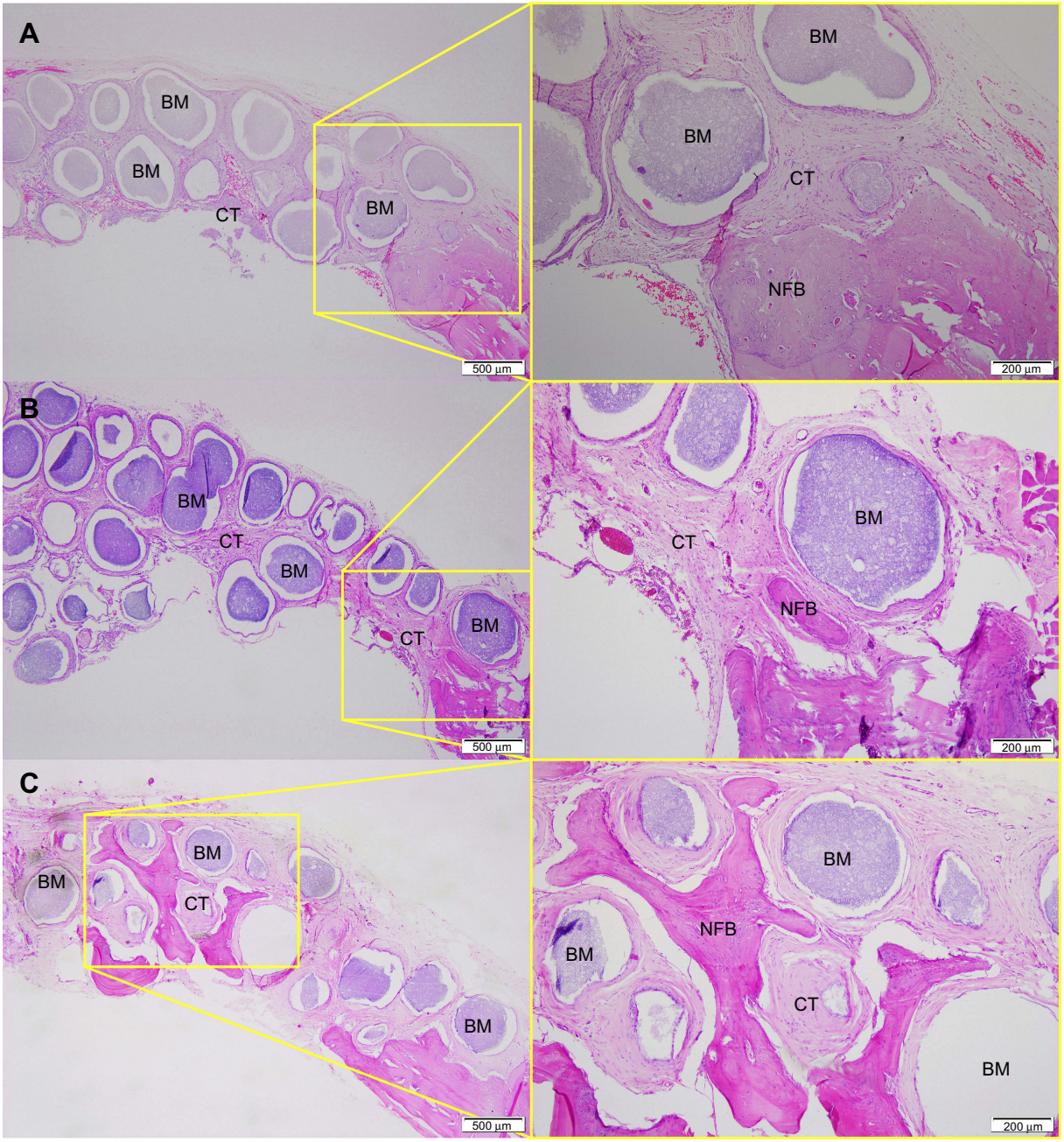

Figure 5 Micrographs of cHA group after 1 (**A**), 3 (**B**) and 6 (**C**) months of implantation, respectively.
Notes: Magnification: 10X. The squares indicate the magnified area observed using a 40X objective. BM, Biomaterial; NFB, New Formed Bone; CT, Connective Tissue. Stain: HE.
Abbreviations: cHA, carbonated hydroxyapatite; HE, hematoxylin-eosin.

biomaterial were found in all extensions of the defect for both groups (Figures 5B and 6B). At the end of 6 months after implantation, small amounts of new bone were found to be associated with the biomaterials, close to the original bone in the defect border. Thick connective tissues, rich in collagen fibers, filled the centers of the defects (Figures 5C and 6C). Irrespective of the experimental periods and biomaterials tested, no signs of biomaterial degradation or fragmentation were evident at the microscopic level.

The histomorphometric analyses showed no effect of time or treatment (biomaterial tested) on the volume density of new bone, which was approximately 1% after 6 months. Throughout the experimental period, the volume density of connective tissue increased ($p<0.0001$) from 39.27% (range: 14.57–58.70%) to 57.09% (range: 19.43–81.78%) in the cHA group. On the other hand, the volume density in this same group decreased ($p=0.0136$) from 49.8% (range: 0.0–76.5%) to

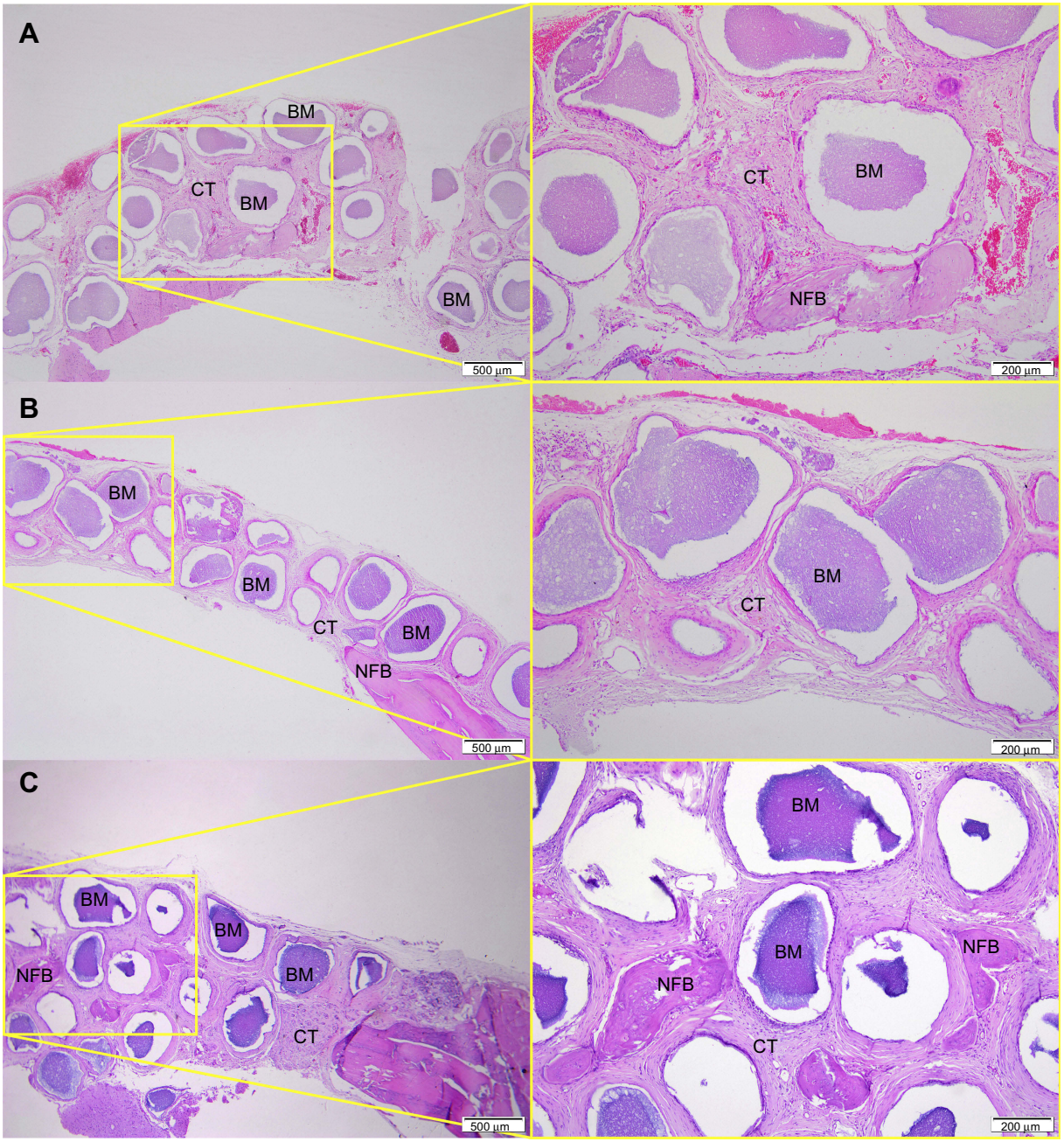

Figure 6 Micrographs of Zn-cHA group after 1 (**A**), 3 (**B**) and 6 (**C**) months of implantation, respectively.
Notes: Magnification: 10X. The squares indicate the magnified area observed using a 40X objective. BM, Biomaterial; NFB, New Formed Bone; CT, Connective Tissue. Stain: HE.
Abbreviations: Zn-cHA, Zinc-doped carbonated hydroxyapatite; HE, hematoxylin-eosin.

36.03% (range: 1.62–70.0%). However, the volume densities of connective tissue and biomaterial did not change throughout the experimental period in the Zn-cHA group.

In vivo CHA and Zn-cHA degradation and Zn bioavailability

The in vivo degradation of the microspheres implanted for 6 months was investigated at the micro- and nanoscales, using SR-µXRF and TEM. SR-µXRF detected variations in the Ca, P, and Zn concentrations in the microsphere vicinity, whereas TEM identified nanoparticle agglomerates released into the medium.

SR-µXRF analyses were conducted in the center of the defect (region 1) and close to the preexisting bone at the defect extremity (region 2). Polarized light microscopy analyses of the cHA and Zn-cHA microspheres situated

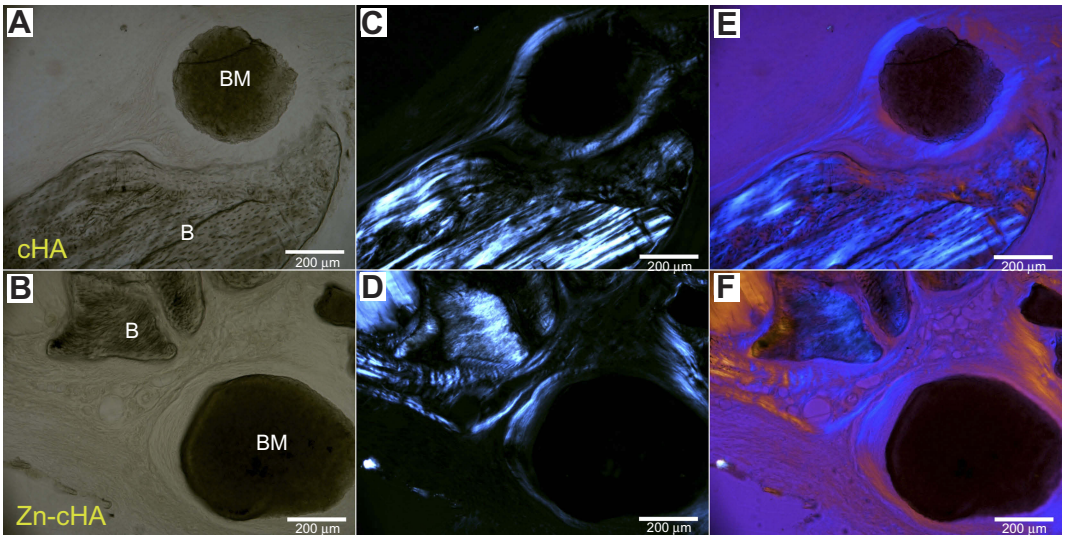

Figure 7 Brightfield and polarized light microscopy images of cHA and Zn-cHA spheres in region 2. (**A,B**) Bright field, (**C,D**) polarized, and (**E,F**) polarized light microscopy with compensator of cHA and Zn-cHA respectively.**Notes:** Magnification: 20X. BM, Biomaterial; B, Bone.
Abbreviations: cHA, carbonated hydroxyapatite; Zn-cHA, Zinc-doped carbonated hydroxyapatite.

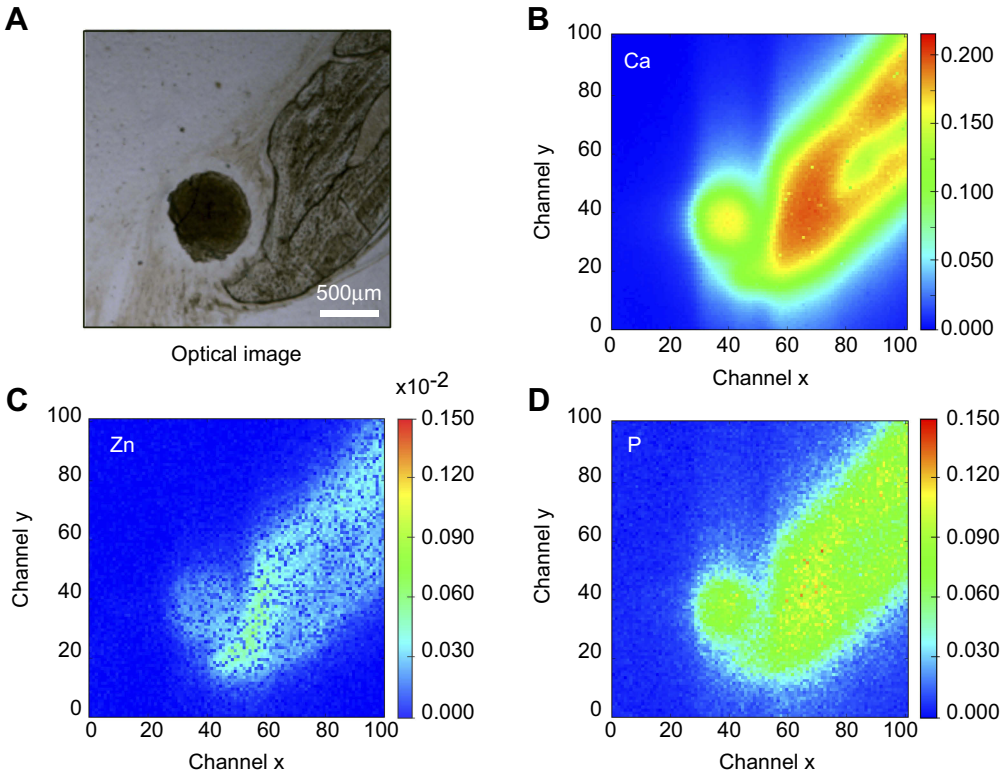

Figure 8 cHA microspheres implanted for 6 months in rat calvaria (region 2). (**A**) Optical image, (**B**–**D**) Ca, Zn and *P* SR-µXRF elemental mapping.
Abbreviations: cHA, carbonated hydroxyapatite; SR-µXRF, Synchrotron radiation-based X-ray microfluorescence.

in region 2 provided evidence of the formation of new bone from the preexistent bone. Structures in the early stages of mineralization (possibly mineralized collagen) were found around the microspheres, linking the preexisting bone to the microspheres. Of note was the absence of organized new bone connecting the preexisting bone to the microspheres after 6 months of implantation (Figure 7A–F).

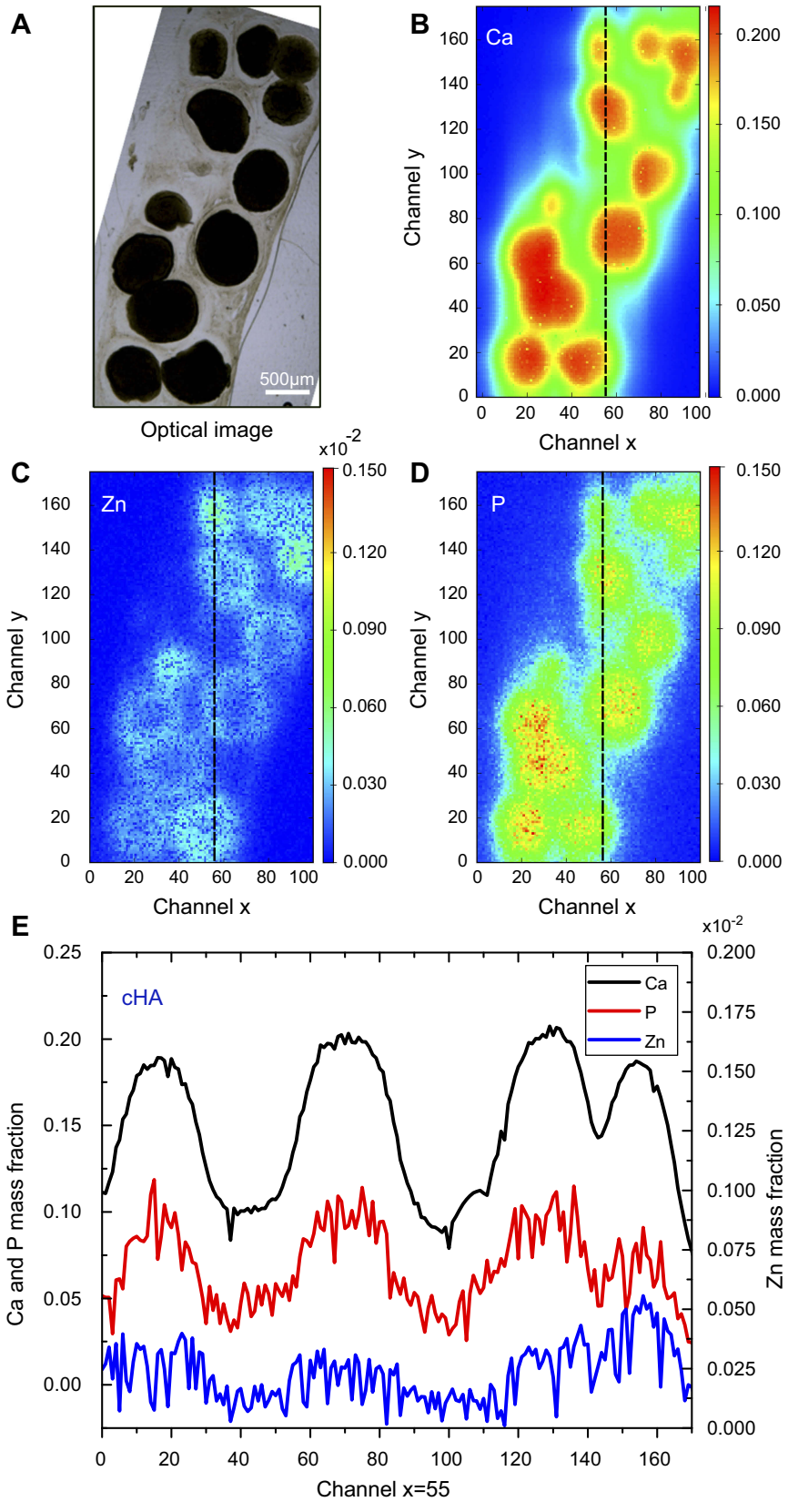

Figure 9 cHA microspheres implanted for 6 months in rat calvaria (region 1). (**A**) Optical image and (**B**–**D**) Ca, Zn and P SR-µXRF elemental mapping; (**E**) Mass fraction profile of Ca, P and Zn along channel 55 (dash lines).
Notes: Dash lines: vertical channel 55.
Abbreviations: cHA, carbonated hydroxyapatite; SR-µXRF, Synchrotron radiation-based X-ray microfluorescence.

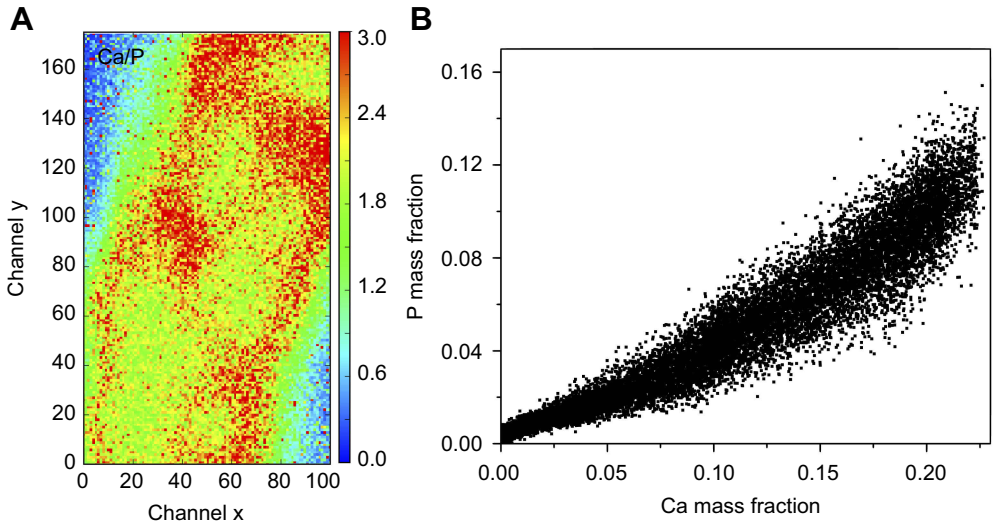

Figure 10 cHA microspheres implanted in rat calvaria for 6 months (region 1): (**A**) Ca/P ratio and (**B**) Ca and *P* mass fraction distribution.
Abbreviation: cHA, carbonated hydroxyapatite.

The SR-μXRF spectra of the defect implanted with cHA microspheres showed major peaks of Ca, P, and Zn, and minor peaks of impurities due to the interaction of the X-ray with air (Ar), and the sample preparation process (Fe) (Figure S2). The elemental mapping (regions 1 and 2) revealed high amounts of Ca and P outside of the microspheres (Figures 8A–D and 9A–D); that is, 50% of the amounts observed in the microsphere interior (as shown in the Ca, P, and Zn elemental profiles in Figure 9E). This high level of Ca could be due to material degradation and local mineralization in the microsphere neighborhood.

In the first case, the material was degraded and high amounts of Ca and P were released into the biological medium throughout the experimental period. Part of the ions was not absorbed by the body and was retained in the neighborhood of the microspheres. Figure 10A,B show a mapping of the Ca/P ratio in region 1. It is worth noting that this ratio increased in regions outside of the microsphere, indicating non-stoichiometric P and Ca resorption in the biological fluid. Although the cHA microspheres did not contain Zn, it was found near the microspheres and also associated with them. The amount of Zn associated with the microspheres was similar to that linked to the old calvarial bone and 10 times higher than the Zn background found in areas far from the implanted materials (Figure 8C).

Optical images of regions 1 and 2 of the rat calvaria implanted with Zn-cHA microspheres are shown in Figures 11A and 12A. No new bone was found in the neighborhood of the Zn-cHA microspheres. The elemental maps of the Ca and P mass fractions followed a similar profile as those in the cHA group (Figures 11B,D and 12B,D). The microsphere neighborhood showed high amounts of Ca, P, and Zn (Figures 11B–D and 12B-D). These elements were very well distributed, with a nearly constant Zn/Ca ratio (Figure 13A), similar to the interior of the microsphere, as shown in the Zn and Ca mass profiles and Zn and Ca distributions (Figures 12E and 13B). A high content of Zn was found in the interior of the Zn-cHA microspheres, with a Zn/Ca ratio close to that of the Zn-cHA powder (~0.05), suggesting that the material preserved its original chemical structure after implantation.

TEM analyses were carried out with ultrathin (~70 nm) sections of the microsphere-implanted defects (6 months) in regions close to the microsphere surface. Figure 14A,D show the interior of the cHA and Zn-cHA microspheres, respectively. The rings from the SAED pattern corresponded to 0.34 nm (most internal) and 0.28 nm (most external), which were related to the 002 and 211 planes from HA, respectively. The interior of the microspheres was formed by particle aggregates and spaces without inorganic material, with sizes lower than 600 nm. At the surface (Figure 14B,C,E, and F), needle-like particles and aggregates were detached from the microspheres and dispensed into the biological medium. This effect occurred mostly in the Zn-cHA sample, where small needle-shaped particles were observed outside of the microspheres (Figure 14F).

Discussion

Bone grafts based on non-ceramic HA with ionic substitution have been proposed for the purpose of combining high osteoconductivity and in vivo resorption. The effect of Zn

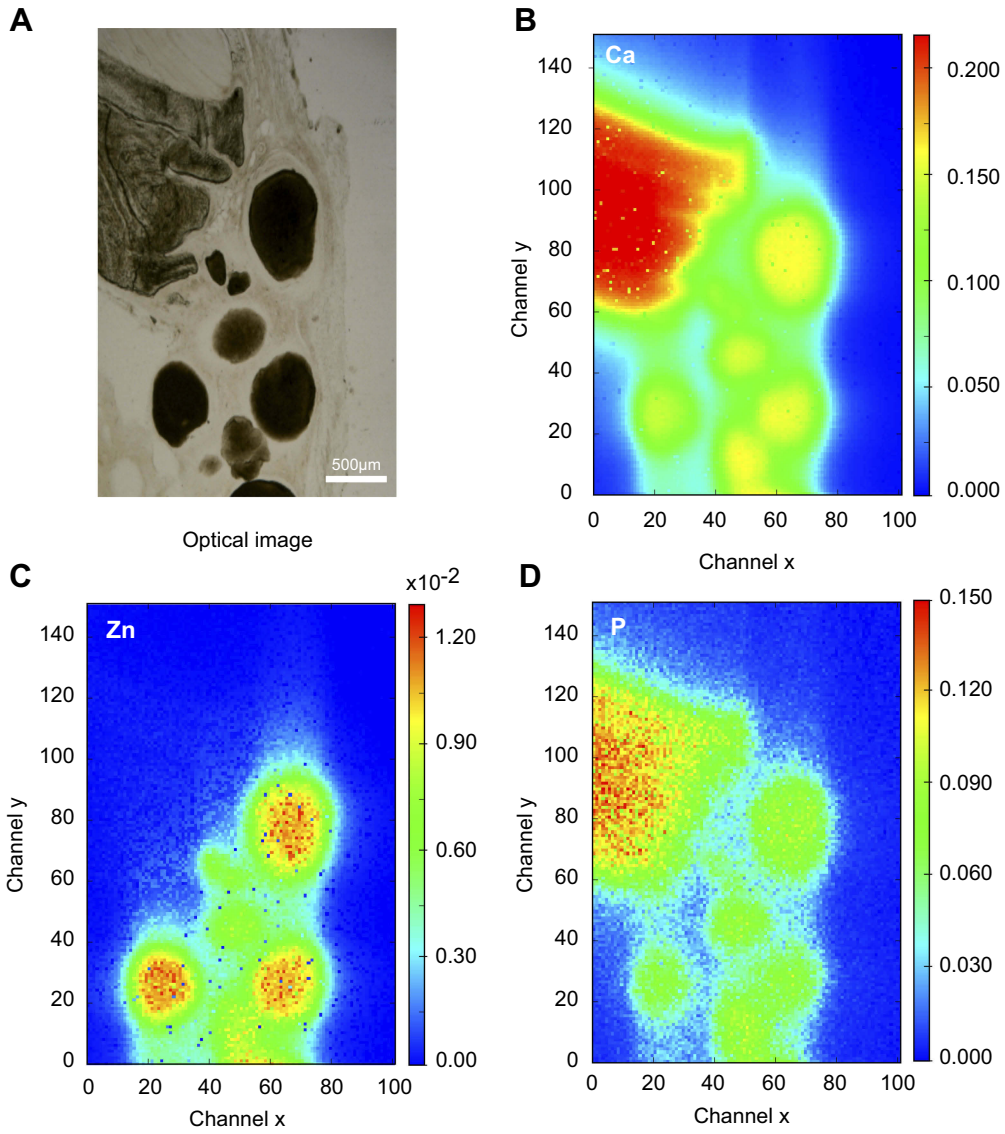

Figure 11 Zn-cHA microspheres implanted for 6 months in rat calvaria (region 2): (**A**) Optical image and (**B**–**D**) Ca, Zn and *P* SR-µXRF elemental mapping.
Abbreviations: Zn-cHA, Zn-doped carbonated hydroxyapatite; SR-µXRF, Synchrotron radiation-based X-ray microfluorescence.

substitution in HA compared with that of ceramic HA on bone repair and osteoconduction is still controversial, as mentioned in prior studies.[10,16,20,22] Out of 14 in vivo studies conducted with Zn-doped CPs (HA and tricalcium phosphate), nine concluded that the association with Zn improved bone repair, whereas the other five studies did not verify any differences between the non-doped and doped biomaterials.[10] It is thus clear that a better understanding of the role of Zn on HA bioactivity is still dependent on comparative investigations using standardized conditions with regard to material preparation, Zn concentrations, animal models, experimental periods, and in vivo degradation of Zn-doped and non-doped CPs.

In the present study, nanocrystalline Zn-cHA and non-doped cHA microspheres were prepared under the same experimental conditions, such as carbonate content, precipitation temperature and pH, and ageing time. Synthesis of the nanostructured powder should be carried out at a high temperature (90 °C) and with a low carbonate content in order to produce crystalline structures without a high dissolution rate. As described elsewhere, Zn incorporation in the apatite structure contributed to a decrease in the sample's crystallinity and particle size.[46–48] It is known that the in vivo Zn bioavailability depends on the Zn concentration, especially the dissolution rate of the CP structure.[10] A low Zn content (<1 wt%) associated with a soluble CP (eg, tricalcium phosphate) was

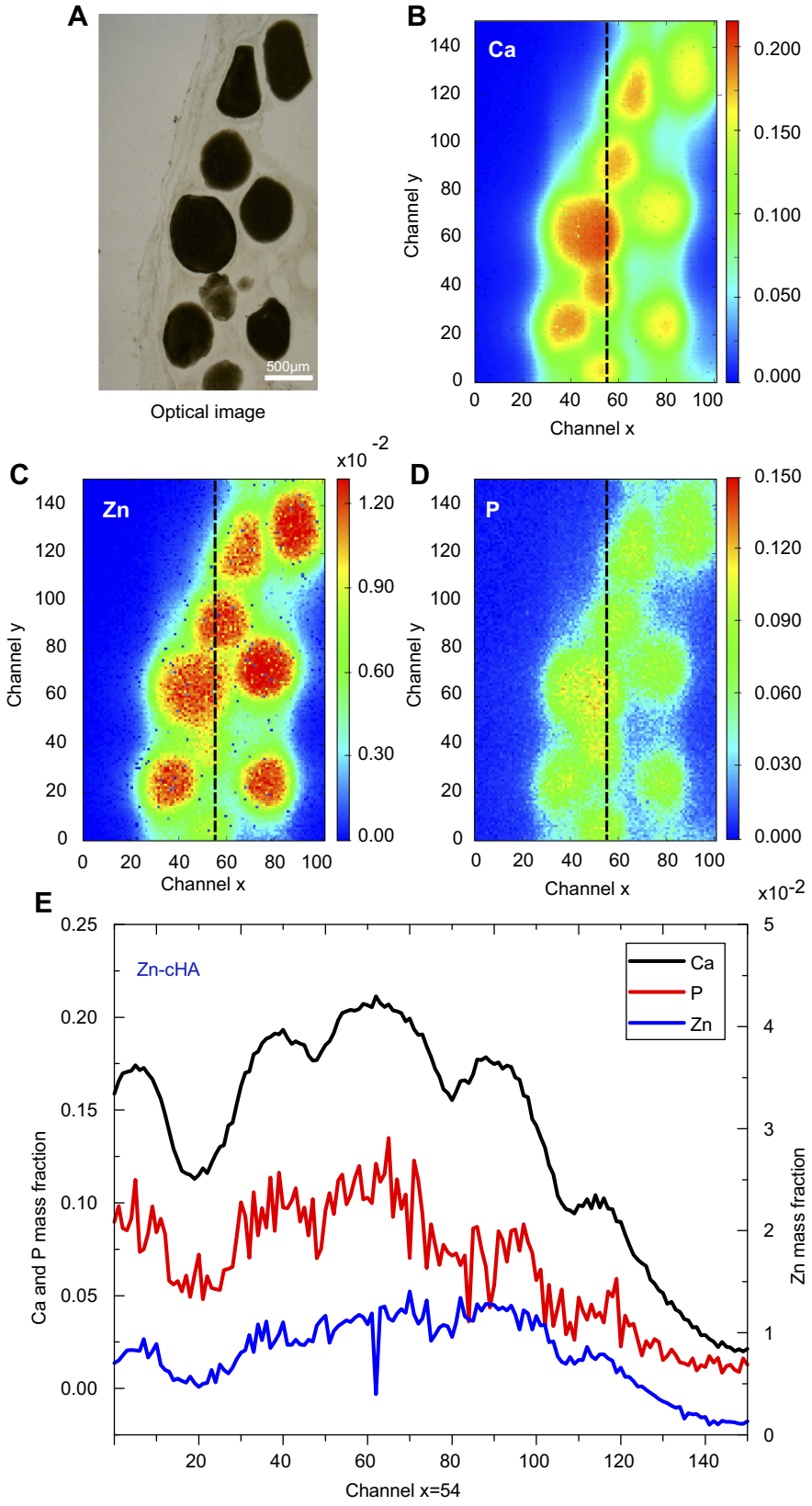

Figure 12 Zn-cHA microspheres implanted for 6 months in rat calvaria (region 1): (**A**) Optical image and (**B**–**D**) Ca, Zn and *P* SR-μXRF elemental mapping, (**E**) Mass fraction profile of Ca, P and Zn along channel 54 (dash lines).

Notes: Dash lines: vertical channel 54.

Abbreviations: Zn-cHA, Zn-doped carbonated hydroxyapatite; SR-μXRF, Synchrotron radiation-based X-ray microfluorescence.

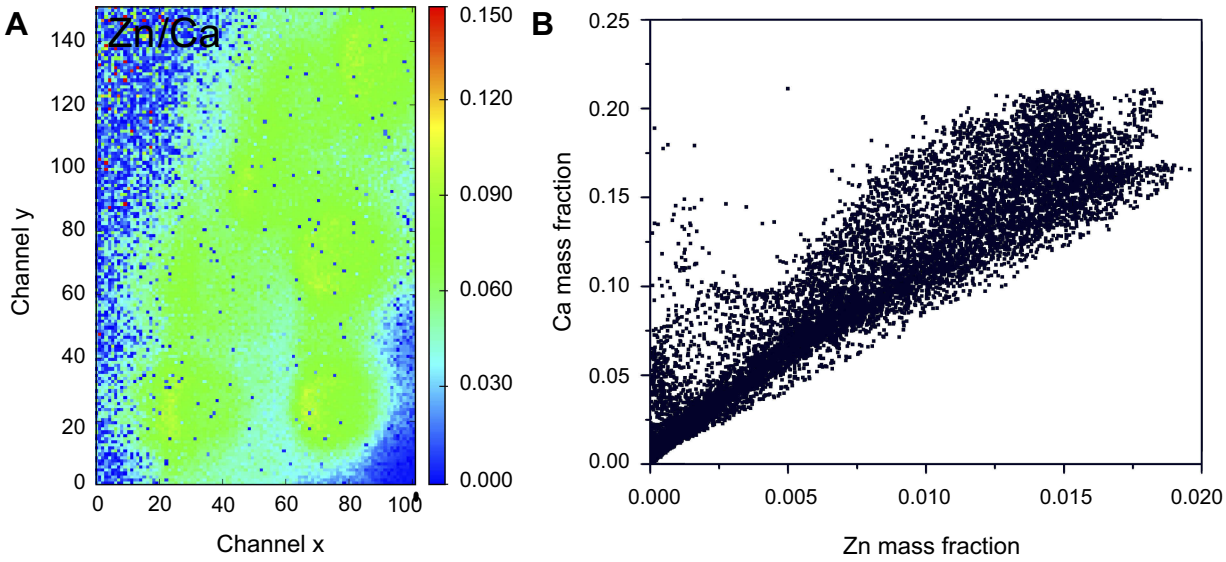

Figure 13 Zn-cHA microspheres implanted in rat calvaria implanted for 6 months (region 1): (**A**) Ca/Zn ratio and (**B**) Ca and Zn mass fraction distribution.
Abbreviation: Zn-cHA, Zn-doped carbonated hydroxyapatite.

implanted in non-critical defects of rats and rabbits, with a positive effect on bone repair.[13] Encouraging results were also obtained using Zn-doped HA with 3.2 wt% of Zn in rat critical-sized defects.[20]

In this present work, Zn-doped cHA with a Zn content of 3.2 wt% was selected to assure a reasonable amount of in vivo Zn release into the biological fluid. The nanostructured powders showed a low carbonate content, and the Zn incorporation into the cHA structure (3.2 wt%) was close to the expected theoretical value. Although cHA and Zn-cHA presented similar crystalline orders, average crystallite sizes, and specific surface areas, cHA was more calcium deficient than Zn-cHA. In the biomaterial fabrication, sodium alginate polymer was used for various reasons: i) it is biocompatible, ii) it stabilizes the spherical shape of the material, iii) it is bioabsorbable in the biological medium, and iv) it allows the generation of nanoporosity in the microspheres after its in vivo implantation.

With SR-μCT analysis, it was possible to characterize the distribution of nanoparticles in the interior of the microsphere as well as the space occupied by the biopolymer. Despite the use of the same preparation procedure, the cHA/alginate microspheres had a larger pore volume and more interconnected micropores than those of the Zn-cHA/alginate microspheres. This effect was attributed to the smaller particle and pore sizes of Zn-cHA powder, as shown in the BET results of Table 1 and the TEM images of Figure 14.

The cHA and Zn-cHA microspheres did not alter the viability of MC3T3-E1 cells in vitro; moreover, the cell metabolic activity was improved when in contact with extracts of the cHA and Zn-cHA microspheres. The release of Ca and Zn from the microspheres may have been responsible for this unexpected cell behavior.

The experimental model used to evaluate bone repair was the critical-sized calvarial defect of the rat. Wistar rats were selected because of their low cost, easy maintenance and handling, and allowance of the standardization of experimental conditions in genetically similar animals. The critical-sized calvarial defect of the rat is one of the most commonly used experimental models for the evaluation of bone repair. It has many advantages, such as the natural inertia of the skull,[49] standardization of the defect size, adequate surgical access, and support for the implantation of biomaterials owing to the presence of dura mater and overlying skin.

Histological evaluations at 1, 3, and 6 months confirmed the biocompatibility of the Zn-cHA and cHA microspheres, as was evident by the discrete presence of inflammatory cells, the absence of tissue necrosis points, and direct bone apposition onto the microspheres. The histological and histomorphometric analyses revealed that bone repair started at the border of the defect from the preexistent bone, with low adhesion to the microspheres and no progression to the center of the defect. This behavior resulted in a small amount of newly formed bone around the defect for both biomaterials. Connective tissue occupied the space around the microspheres, as evident from the limited osteoconductivity of both biomaterials.

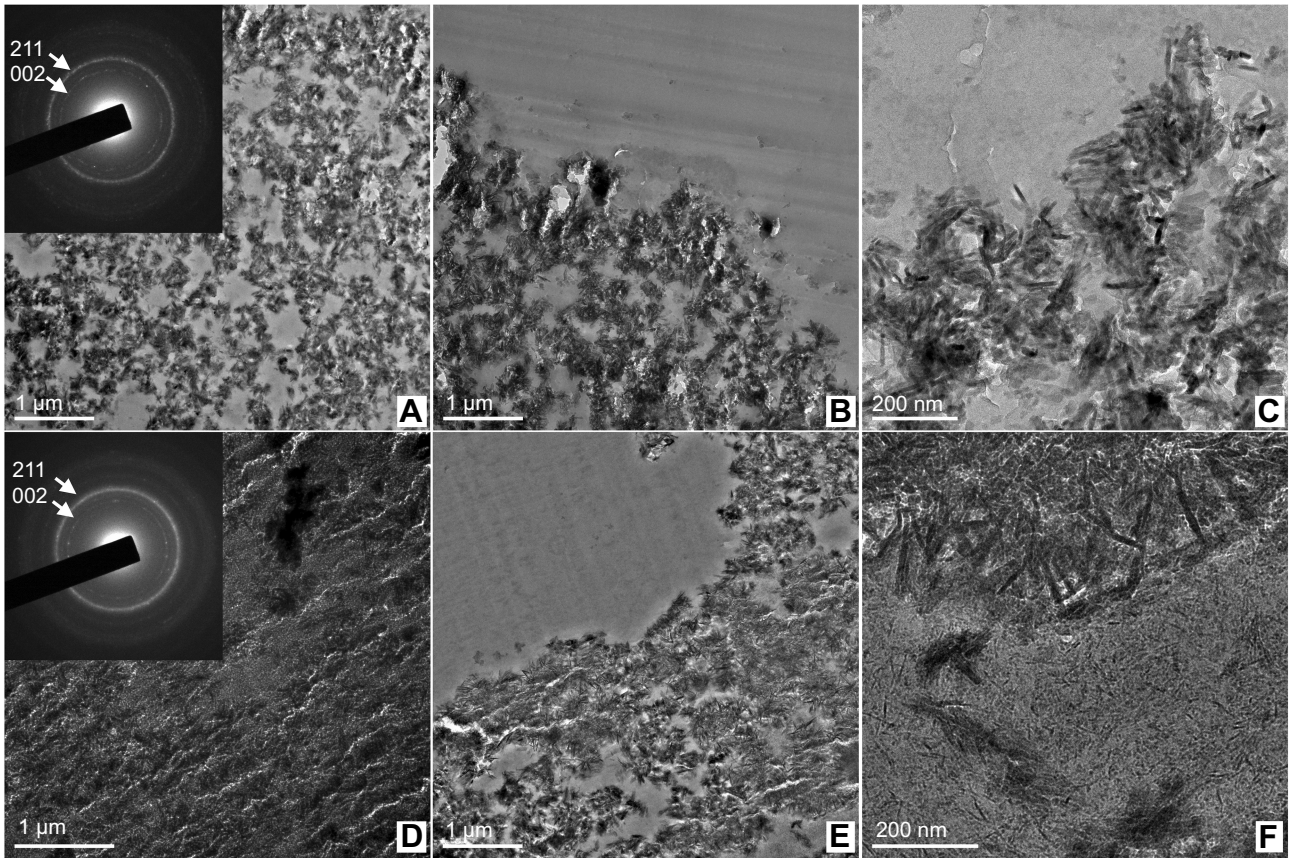

Figure 14 TEM image shows nanoscale regions of the microsphere interior and the surface in contact with the biological medium, (**A**–**C**) cHA and (**D**–**F**) Zn-cHA. Insert: SAED patterns with labeled Miller indices of each ring.
Abbreviations: TEM, Transmission electron microscopy; cHA, Carbonated hydroxyapatite; Zn-cHA, Zn-doped carbonated hydroxyapatite; SAED, Selected area electron diffraction.

The resultant bone repair was quite limited for both materials, despite the presence of Zn and the existence of micropores and pore interconnectivity that enabled the flux of biological fluids and cells through the microspheres. This effect could be associated with the high levels of Ca^{2+} around the microspheres, in both cHA and Zn-cHA, as detected by SR-µXRF.

SR-µXRF analyses revealed some clues for understanding the low osteoconductive behavior of the cHA and Zn-cHA microspheres implanted in the critical bone defects. One clue was the weak microsphere fragmentation after implantation. According to previous studies, low fragmentation does not favor osteoconduction, but also does not prevent new bone adhesion to HA for long implantation times.[9,19] The second clue was the excess amounts of Ca, P, and Zn released from the nanostructured cHA and Zn-cHA microspheres and their spread throughout the defect region, especially to the tissue around the microspheres. The liberation of Ca and Zn was so high that it exceeded the body's ability to reabsorb these elements. The SR-µXRF analyses confirmed that alginate did not impact the in vivo dissolution of the cHA and Zn-cHA particles. The alginate dissolution generated pores within the microspheres, facilitating the flow of Ca, P, and Zn to the exterior. The small particle size and the high specific surface area of the nanomaterials were also decisive parameters for the elevated Ca, P, and Zn dissolution rates. The Ca/P ratios in the defect, compared with those in the microsphere interior, reinforced the partial dissolution of the cHA nanoparticles and the non-stoichiometric reabsorption of P and Ca in the biological fluid (Figure 11). The possibility of local mineralization of collagen in the neighborhood of the microspheres cannot be ruled out. Outside of the Zn-cHA microspheres, the mass distribution profile of Zn was similar to that of calcium, thus confirming the high Zn mobility and the nearly stoichiometric release of the two elements. Although Zn was spread throughout the defective region, it was not associated with the preexistent calvarial bone. Besides ionic dissolution, nanoparticle agglomerates were also released into the biological fluid, as indicated by TEM. The maintenance of high levels of Ca^{2+} ions in the surrounding medium, as evidenced by SR-µXRF,

could explain the impairment of bone growth and connective tissue formation. A high level of extracellular Ca induces prostaglandin E2 synthesis, which strongly affects bone metabolism[50,51] and increases osteoclastogenesis.[52,53]

Conclusion

Nanostructured cHA/alginate microspheres and Zn-doped cHA/alginate microspheres were implanted in critical-sized calvarial defects in rats. Although the nanomaterials were cytocompatible and biocompatible, they showed limited osteoconductivity independent of the Zn in cHA. Elemental mapping based on SR-μXRF enabled characterization of the in vivo degradation of the cHA and Zn-cHA microspheres. The high level of Ca and Zn released from the microspheres into the defect, and the low clearance of these metals in the biological fluid, played critical roles in the inhibition of osteoconduction and the subsequent impairment of bone repair. Effective control of the dissolution rate is a critical issue for the design of efficient nanostructured calcium phosphate grafts for bone regeneration.

Acknowledgments

This work was supported by the Brazilian financial agencies CNPq (Grant no 457541/2013-0 and 467513/2014-7), FAPERJ (Grant no E-26/102.993/2012; E-26/203.012/2016), and Coordenação de Aperfeiçoamento de Pessoal de Nível Superior - Brasil (CAPES) (Finance Code 001), National Centre of Science and Technology on Regenerative Medicine - INCT Regenera (http://www.inctregenera.org.br/). The authors wish to thank LABNANO/CBPF, the staff of the IMX and XRF beamlines of the Brazilian Synchrotron Light Laboratory (LNLS), and Carlos Perez (XRF Beamline, LNLS) and Professor Marcos Farina (Federal University of Rio de Janeiro, UFRJ) for their invaluable contributions to this work.

Disclosure

The authors report no conflicts of interest in this work.

References

1. Goldberg M, Langer R, Jia X. Nanostructured materials for applications in drug delivery and tissue engineering. *J Biomater Sci Polym Ed*. 2007;18(3):241–268.
2. Sun F, Zhou H, Lee J. Various preparation methods of highly porous hydroxyapatite/polymer nanoscale biocomposites for bone regeneration. *Acta Biomater*. 2011;7(11):3813–3828. doi:10.1016/j.actbio.2011.07.002
3. Ghorbani FM, Kaffashi B, Shokrollahi P, Seyedjafari E, Ardeshirylajimi A. PCL/chitosan/Zn-doped nHA electrospun nanocomposite scaffold promotes adipose derived stem cells adhesion and proliferation. *Carbohydr Polym*. 2015;118:133–142. doi:10.1016/j.carbpol.2014.10.071
4. Gong T, Xie J, Liao J, Zhang T, Lin S, Lin Y. Nanomaterials and bone regeneration. *Bone Res*. 2015;3:15029.
5. Wang P, Zhao L, Liu J, Weir MD, Zhou X, Xu HHK. Bone tissue engineering via nanostructured calcium phosphate biomaterials and stem cells. *Bone Res*. 2014;2:14017.
6. Najafinezhad A, Abdellahi M, Saber-Samandari S, Ghayour H, Khandan A. Hydroxyapatite- M-type strontium hexaferrite: a new composite for hyperthermia applications. *J Alloys Compd*. 2018;734:290–300. doi:10.1016/j.jallcom.2017.10.138
7. Sahmani S, Saber-Samandari S, Shahali M, et al. Mechanical and biological performance of axially loaded novel bio-nanocomposite sandwich plate-type implant coated by biological polymer thin film. *J Mech Behav Biomed Mater*. 2018;88(June):238–250. doi:10.1016/j.jmbbm.2018.08.030
8. Šupová M. Substituted hydroxyapatites for biomedical applications: a review. *Ceram Int*. 2015;41(8):9203–9231. doi:10.1016/j.ceramint.2015.03.316
9. Calasans-Maia M, Calasans-Maia J, Santos S, et al. Short-term in vivo evaluation of zinc-containing calcium phosphate using a normalized procedure. *Mater Sci Eng C*. 2014;41:309–319. doi:10.1016/j.msec.2014.04.054
10. Cruz R, Calasans-Maia J, Sartoretto S, et al. Does the incorporation of zinc into calcium phosphate improve bone repair? A systematic review. *Ceram Int*. 2018;44(2):1240–1249. doi:10.1016/j.ceramint.2017.10.157
11. Calasans-Maia M, Fernandes GVO, Rossi AM, et al. Effect of hydroxyapatite and zinc-containing hydroxyapatite on osseous repair of critical size defect in the rat calvaria. *Key Eng Mater*. 2007;361–363:1273–1276. doi:10.4028/www.scientific.net/KEM.361-363.1273
12. Calasans-Maia M, Rossi AM, Dias EP, Santos SRA, Áscoli F, Granjeiro JM. Stimulatory effect on osseous repair of zinc-substituted hydroxyapatite: histological study in rabbit's tibia. *Key Eng Mater*. 2007;361–363:1269–1272. doi:10.4028/www.scientific.net/KEM.361-363.1269
13. Kawamura H, Ito A, Miyakawa S, et al. Stimulatory effect of zinc-releasing calcium phosphate implant on bone formation in rabbit femora. *J Biomed Mater Res*. 2000;50(2):184–190.
14. Kawamura H, Ito A, Miyakawa S, Ojima K, Ichinose N, Tateishi T. Effects of zinc-releasing calcium phosphate ceramics implanted in rabbit femora. *Key Eng Mater*. 2000;192–195:387–390. doi:10.4028/www.scientific.net/KEM.192-195.387
15. Kawamura H, Ito A, Muramatsu T, Miyakawa S, Ochiai N, Tateishi T. Long-term implantation of zinc-releasing calcium phosphate ceramics in rabbit femora. *J Biomed Mater Res*. 2003;65A(4):468–474. doi:10.1002/(ISSN)1097-4636
16. Chou J, Hao J, Kuroda S, et al. Bone regeneration of rat tibial defect by zinc-tricalcium phosphate (Zn-TCP) synthesized from porous foraminifera carbonate macrospheres. *Mar Drugs*. 2013;11(12):5148–5158. doi:10.3390/md11125148
17. Calasans-Maia M, Sales E, Granjeiro JM, et al. Bone implant interface investigation by synchrotron radiation X-ray microfluorescence. *AIP Conference Proceedings*. Vol 1221;2010:160–163.
18. Yu W, Sun T-W, Qi C, et al. Evaluation of zinc-doped mesoporous hydroxyapatite microspheres for the construction of a novel biomimetic scaffold optimized for bone augmentation. *Int J Nanomedicine*. 2017;12:2293–2306. doi:10.2147/IJN.S126505

19. Resende RFB, Fernandes GVO, Santos SRA, et al. Long-term biocompatibility evaluation of 0.5 % zinc containing hydroxyapatite in rabbits. *J Mater Sci Mater Med*. 2013;24(6):1455–1463. doi:10.1007/s10856-013-4865-x
20. Fernandes GVO, Calasans-Maia M, Mitri FF, et al. Histomorphometric analysis of bone repair in critical size defect in rats calvaria treated with hydroxyapatite and zinc-containing hydroxyapatite 5%. *Key Eng Mater*. 2008;396–398:15–18. doi:10.4028/www.scientific.net/KEM.396-398
21. Suruagy AAP, Alves AT, Sartoretto SC, Calasans-Maia JDA, Granjeiro JM, Calasans-Maia MD. Physico-chemical and histomorphometric evaluation of zinc-containing hydroxyapatite in rabbits calvaria. *Braz Dent J*. 2016;27(6):717–726. doi:10.1590/0103-6440201601028
22. Nascimento L, Medeiros M, Calasans-Maia J, et al. Osseoinduction evaluation of hydroxyapatite and zinc containing hydroxyapatite granules in rabbits. *Key Eng Mater*. 2011;493–494:252–257. doi:10.4028/www.scientific.net/KEM.493-494.252
23. Luo X, Barbieri D, Davison N, Yan Y, de Bruijn JD, Yuan H. Zinc in calcium phosphate mediates bone induction: in vitro and in vivo model. *Acta Biomater*. 2014;10(1):477–485. doi:10.1016/j.actbio.2013.10.011
24. Brunauer S, Emmett PH, Teller E. Adsorption of gases in multimolecular layers. *J Am Chem Soc*. 1938;60(2):309–319. doi:10.1021/ja01269a023
25. Barrett EP, Joyner LG, Halenda PP. The determination of pore volume and area distributions in porous substances. I. Computations from nitrogen isotherms. *J Am Chem Soc*. 1951;73(1):373–380. doi:10.1021/ja01145a126
26. Pérez CA, Radtke M, Sánchez HJ, et al. Synchrotron radiation X-ray fluorescence at the LNLS: beamline instrumentation and experiments. *X-Ray Spectrom*. 1999;28(5):320–326. doi:10.1002/(SICI)1097-4539(199909/10)28:5<320::AID-XRS359>3.0.CO;2-1
27. Zhang L, Hustache R, Hignette O, Ziegler E, Freund A. Design optimization of a flexural hinge-based bender for X-ray optics. *J Synchrotron Radiat*. 1998;5(3):804–807. doi:10.1107/S0909049597015288
28. Pérez CA, Murari JFJ, Moreno GBZL, Da Silva JL, Piton JR. Development of fast scanning X-ray fluorescence microscopy at the LNLS D09B-XRF beamline. *AIP Conference Proceedings*. Vol 1764. AIP Publishing LLC; 2016:030001.
29. Solé VA, Papillon E, Cotte M, Walter P, Susini J. A multiplatform code for the analysis of energy-dispersive X-ray fluorescence spectra. *Spectrochim Acta Part B At Spectrosc*. 2007;62(1):63–68. doi:10.1016/j.sab.2006.12.002
30. Broll N. Quantitative x-ray fluorescence analysis. Theory and practice of the fundamental coefficient method. *X-Ray Spectrom*. 1986;15(4):271–285. doi:10.1002/xrs.1300150410
31. Lima I, Anjos MJ, Fleiuss MLF, Rosenthal D, Lopes RT. Characterization of osteoporotic bone structures by bidimensional images through x-ray microfluorescence with synchrotron radiation. *X-Ray Spectrom*. 2008;37(3):249–254. doi:10.1002/xrs.986
32. Herbert Attix F. *Introduction to Radiological Physics and Radiation Dosimetry*. John Wiley; Sons Inc, ed. Strauss GmbH, Morlenbach: Wiley-VCH Verlag GmbH & Co. KGaA; 1986. Available from: http://dnb.ddb.de. Accessed December 12, 2018.
33. Brooks RA, Di CG. Beam hardening in X-ray reconstructive tomography. *Phys Med Biol*. 1976;21(3):004. doi:10.1088/0031-9155/21/3/004
34. Miqueles EX, Helou ES. Fast backprojection operator for synchrotron tomographic data. *Progress in Industrial Mathematics at ECMI 2014*. Springer, Cham; 2016:243–252.
35. Koshev N, Helou ES, Miqueles EX. Fast backprojection techniques for high resolution tomography. August 2016:1–32. Available from: http://arxiv.org/abs/1608.03589. Accessed November 12, 2018.
36. Miqueles EX, Helou ES, De Pierro AR. Generalized backprojection operator: fast calculation. *J Phys Conf Ser*. 2014;490(1):012148. doi:10.1088/1742-6596/490/1/012148
37. Schindelin J, Arganda-Carreras I, Frise E, et al. Fiji: an open-source platform for biological-image analysis. *Nat Methods*. 2012;9(7):676–682. doi:10.1038/nmeth.2019
38. Buades A, Coll B, Morel J-M A non-local algorithm for image denoising. *2005 IEEE Computer Society Conference on Computer Vision and Pattern Recognition (CVPR'05)*. Vol 2. IEEE:60–65.
39. Lin G, Adiga U, Olson K, Guzowski JF, Barnes CA, Roysam B. A hybrid 3D watershed algorithm incorporating gradient cues and object models for automatic segmentation of nuclei in confocal image stacks. *Cytometry*. 2003;56A(1):23–36. doi:10.1002/(ISSN)1097-0320
40. Ruspini LC, Farokhpoor R, Øren PE. Pore-scale modeling of capillary trapping in water-wet porous media: a new cooperative pore-body filling model. *Adv Water Resour*. 2017;108:1–14. doi:10.1016/j.advwatres.2017.07.008
41. Raeini AQ, Bijeljic B, Blunt MJ. Generalized network modeling: network extraction as a coarse-scale discretization of the void space of porous media. *Phys Rev E*. 2017;96(1):013312. doi:10.1103/PhysRevE.96.013312
42. ISO 10993-5:2009(en), Biological evaluation of medical devices — part 5: tests for in vitro cytotoxicity. Available from: https://www.iso.org/obp/ui/#iso:std:iso:10993:-5:ed-3:v1:en. Accessed November 28, 2018.
43. Guimarães MV, Da Cruz Freire JE, Bezerra De Menezes LM. Utilização de animais em pesquisas: breve revisão da legislação no Brasil. *Rev Bioét*. 2016;24(2):217–241. doi:10.1590/1983-80422016242121
44. Kilkenny C, Browne W, Cuthill IC, Emerson M, Altman DG. Animal research: reporting in vivo experiments: the ARRIVE guidelines. *Br J Pharmacol*. 2010;160(7):1577–1579. doi:10.1111/j.1476-5381.2010.00872.x
45. Holzwarth U, Gibson N. The Scherrer equation versus the "Debye-Scherrer equation.". *Nat Nanotechnol*. 2011;6(9):534. doi:10.1038/nnano.2011.145
46. Hu W, Ma J, Wang J, Zhang S. Fine structure study on low concentration zinc substituted hydroxyapatite nanoparticles. *Mater Sci Eng C*. 2012;32(8):2404–2410. doi:10.1016/j.msec.2012.07.014
47. Guerra-López JR, Echeverría GA, Güida JA, Viña R, Punte G. Synthetic hydroxyapatites doped with Zn(II) studied by X-ray diffraction, infrared, Raman and thermal analysis. *J Phys Chem Solids*. 2015;81:57–65. doi:10.1016/j.jpcs.2015.01.017
48. Kumar GS, Thamizhavel A, Yokogawa Y, Kalkura SN, Girija EK. Synthesis, characterization and in vitro studies of zinc and carbonate co-substituted nano-hydroxyapatite for biomedical applications. *Mater Chem Phys*. 2012;134(2–3):1127–1135. doi:10.1016/j.matchemphys.2012.04.005
49. Prolo DJ, Gutierrez RV, De Vine JS, Oklund SA. Clinical utility of allogeneic skull discs in human craniotomy. *Neurosurgery*. 1984;14(2):183–186.
50. Leis HJ, Zach D, Huber E, Ziermann L, Gleispach H, Windischhofer W. Extracellular Ca2+ sensing by the osteoblast-like cell line, MC3T3-E1. *Cell Calcium*. 1994;15(6):447–456.
51. Choudhary S, Wadhwa S, Raisz LG, Alander C, Pilbeam CC. Extracellular calcium is a potent inducer of cyclo-oxygenase-2 in murine osteoblasts through an ERK signaling pathway. *J Bone Miner Res*. 2003;18(10):1813–1824. doi:10.1359/jbmr.2003.18.10.1813
52. Shin -M-M, Kim YH, Kim SN, Kim G-S, Baek J-H. High extracellular Ca2+ alone stimulates osteoclast formation but inhibits in the presence of other osteoclastogenic factors. *Exp Mol Med*. 2003;35(3):167–174. doi:10.1038/emm.2003.23
53. Kaji H, Sugimoto T, Kanatani M, Chihara K. High extracellular calcium stimulates osteoclast-like cell formation and bone-resorbing activity in the presence of osteoblastic cells. *J Bone Miner Res*. 1996;11(7):912–920. doi:10.1002/jbmr.5650110707

Supplementary materials

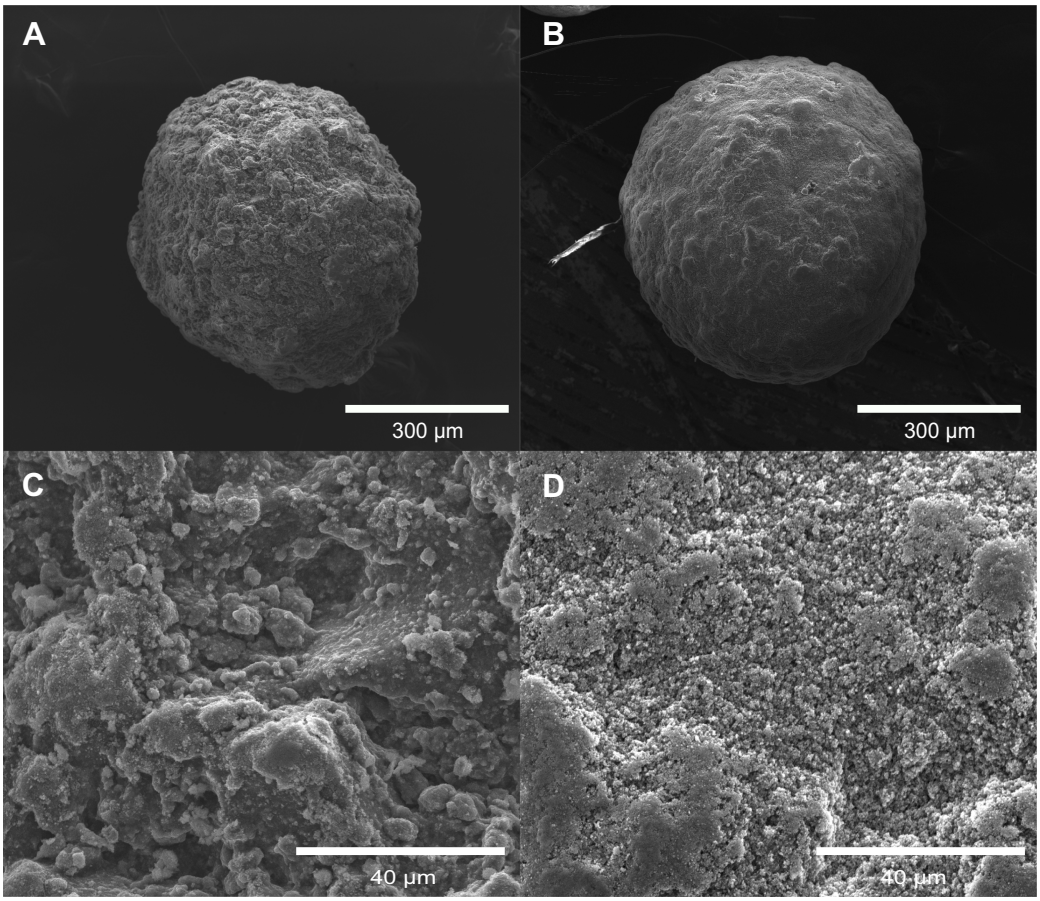

Figure S1 SEM micrographs of cHA and Zn-cHA. (**A**) cHA and (**B**) Zn-cHA microspheres at 300X magnification; (**C**) cHA and (**D**) Zn-cHA microspheres at 3000X magnification.
Notes: 300X magnification, scale bar: 300 µm; 3000X magnification, scale bar: 40 µm.
Abbreviations: SEM, Scanning electron microscopy; cHA, Carbonated hydroxyapatite; Zn-cHA, Zn-doped carbonated hydroxyapatite.

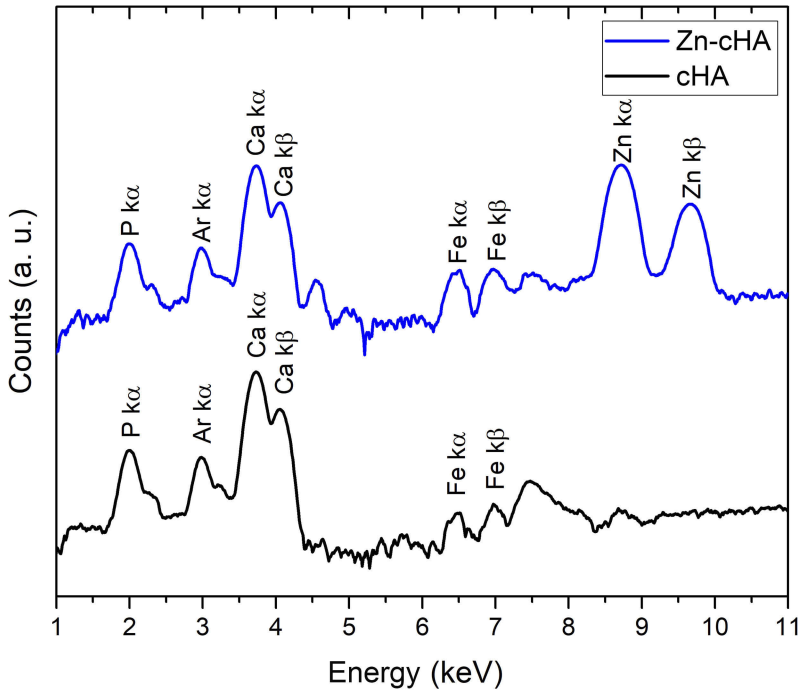

Figure S2 SR-μXRF spectra of cHA and Zn-cHA microspheres (region 1).
Abbreviations: SR-μXRF, Synchrotron radiation-based X-ray microfluorescence; cHA, Carbonated hydroxyapatite; Zn-cHA, Zn-doped carbonated hydroxyapatite.

International Journal of Nanomedicine Dovepress

Publish your work in this journal

The International Journal of Nanomedicine is an international, peer-reviewed journal focusing on the application of nanotechnology in diagnostics, therapeutics, and drug delivery systems throughout the biomedical field. This journal is indexed on PubMed Central, MedLine, CAS, SciSearch®, Current Contents®/Clinical Medicine, Journal Citation Reports/Science Edition, EMBase, Scopus and the Elsevier Bibliographic databases. The manuscript management system is completely online and includes a very quick and fair peer-review system, which is all easy to use. Visit http://www.dovepress.com/testimonials.php to read real quotes from published authors.

Submit your manuscript here: https://www.dovepress.com/international-journal-of-nanomedicine-journal